Wiener chaos expansion method for thermal radiation from inhomogeneous structures

Zhuo Li, Jiayu Li, Xiu Liu, Hakan Salihoglu, and Sheng Shen

Phys. Rev. B **104**, 195426 — Published 22 November 2021

DOI: 10.1103/PhysRevB.104.195426

Wiener-Chaos Expansion Method for Thermal Radiation from Inhomogeneous Structures

Zhuo Li[†], Jiayu Li[†], Xiu Liu[†], Hakan Salihoglu[†], and Sheng Shen*[, †]

[†] Department of Mechanical Engineering, Carnegie Mellon University, Pittsburgh, Pennsylvania 15213, United States

Abstract

The Wiener-Chaos expansion method provides a direct approach to accurately compute the thermal radiation from arbitrary structures. Here, we further extend this method to the structures with a permittivity or temperature inhomogeneity. The inhomogeneous Wiener-Chaos expansion method treats the two kinds of inhomogeneities with the same governing equation and thus provides a systematic solution to the radiative spectra. Compared to the traditional approach that approximates the thermal radiation from an inhomogeneous structure by the superposition of contributions from its quasi-homogenous subparts, our new method calculates the thermal radiation from the entire inhomogeneous structure simultaneously and thus improves the time efficiency. We validate the new method against the traditional approach and apply it to study the near field radiative heat transfer between two gold nanorods with different temperature profiles, from which a four-time tunability is demonstrated at the plasmonic resonance.

Keywords: WCE method, inhomogeneous system, near-field thermal radiation

1. Introduction

Thermal radiation physically originates from photons spontaneously emitted at different positions in a thermal source. On a macroscopic scale, these highly localized photons are usually uncorrelated, leading to quasi-isotropic and incoherent thermal emission. Although thermal radiation from bulk materials is well understood in the context of Planck's law and heat transfer using emissivity, there still remains a significant gap in our understanding of thermal radiation at the subwavelength scale. Due to their sub-wavelength sizes, micro/nanostructures can support localized surface plasmon polaritons [1,2] or surface phonon polaritons [3], leading to narrow band resonance in their far field radiation spectra in contrast to the common broadband response from bulk emitters. In the near field region, radiative heat transfer can break the blackbody radiation limit by orders of magnitude because of the contribution of evanescent waves. As a result, micro/nanostructures are essential to a variety of applications, including optical sensing [4–6], thermophotovoltaics [7–13] and infrared spectroscopy [14–16].

Because Planck's Law cannot be applied to sub-wavelength structures, the formulation of thermal radiation from micro/nanostructures mainly relies on fluctuational electrodynamics. In principle, an analytical solution can be theoretically given with the help of Dyadic Green's functions [17]. However, this is computationally challenging due to the lack of the closed form analytical expression of the Dyadic Green's function for complex geometries. Hence, several theories and methods have been introduced to tackle this issue, including the equivalent circuit theory (ECT) [18], the coupled mode theory (CMT)[19,20], the quasi-normal mode (QNM) theory [21–23], the fluctuational surface current (FSC) method [24,25], and the Wiener-Chaos expansion (WCE) method [26–28]. However, the previous research is mainly focused on homogeneous (or at least piece-wisely homogeneous) structures [29–33], where the material

property and temperature are spatially invariant. Although the fluctuational volume current (FVC) method was introduced to treat micro-emitters with the permittivity or temperature inhomogeneity, only non-dispersive emitters (i.e., the permittivity of the emitter is not a function of frequency) were considered [34].

In this article, we re-formulate the WCE method for inhomogeneous systems. The inhomogeneities in both the permittivity and the temperature are treated simultaneously in the derivation and thus can be solved by the same governing equation. The implementation of the inhomogeneous WCE method is discussed in detail. We validate the new method via studying the radiative spectrum from a layered emitter featured with a piece-wisely homogeneous permittivity. The near field radiative heat transfer between two gold nanorods with a linear temperature gradient is then studied to demonstrate the influence of the non-uniform temperature profile on the radiative heat transfer.

2. Principle of the inhomogeneous WCE method

According to fluctuational electrodynamics, thermal radiation originates from the random current sources induced by the Brownian motion of charges inside an emitter. Consider an emitter enclosing a volume of V with a current source $\vec{j}(\vec{r_1}, \omega)$. The emitted electrical and magnetic fields can be expressed as

$$\vec{E}(\vec{r}_0, \omega) = i\mu_0\omega \int_V G^E(\vec{r}_0, \vec{r}_1)\vec{j}(\vec{r}_1, \omega)\mathrm{d}\,\vec{r}_1, \quad (1)$$

and

$$\vec{H}(\vec{r}_0, \omega) = \int_V G^H(\vec{r}_0, \vec{r}_1)\vec{j}(\vec{r}_1, \omega)d\,\vec{r}_1\,, \quad (2)$$

respectively, where G^E and G^H are the Dyadic Green's functions of the system. The Poynting vector of the emitted electromagnetic field then reads [32]:

$$\langle P_k(\vec{r}_0,\omega)\rangle = \varepsilon_{ijk}\langle E_i H_j\rangle = \varepsilon_{ijk}\cdot i\mu_0\omega\int_V \mathrm{d}\,\vec{r}_1\int_V \mathrm{d}\,\vec{r}_2 \mathrm{Tr}\left[G_i^{E*}G_j^H\langle\vec{j}(\vec{r}_1,\omega)\vec{j}^*(\vec{r}_2,\omega)\rangle\right]$$
$$\equiv \mathrm{L_p}[V;\langle\vec{j}(\vec{r}_1,\omega)\vec{j}^*(\vec{r}_2,\omega)\rangle]. \quad (3)$$

In Eq. (3), $i,j,k \in \{x,y,z\}$, P_k represents the k component of the Poynting vector $\vec{P}$ and ε_{ijk} is the Levi-Civita symbol. Here we define a linear operator $\mathrm{L_p}[\Omega;X]$ associated with the Poynting vector. Ω specifies the domain where the integrations are carried over, and X is a 3 by 3 correlation matrix of the current source. The bra-kets $\langle\cdots\rangle$ represent the ensemble average.

The current source $\vec{j}$ is thermally induced and thus can be quantified by the fluctuation dissipation theorem (FDT) [35]:

$$\langle\vec{j}(\vec{r},\omega)\rangle = 0; \quad (4)$$

$$\langle\vec{j}(\vec{r}_1,\omega)\vec{j}^*(\vec{r}_2,\omega)\rangle = V_E^2(\vec{r}_1,\omega)\delta(\vec{\mathrm{r}}_1-\vec{\mathrm{r}}_2)\boldsymbol{I}. \quad (5)$$

In Eq. (5), $\boldsymbol{I}$ is the 3 by 3 identity and V_E^2 is a non-zero (if the emitter is lossy) deterministic term given by the imaginary part of the permittivity and the temperature of the emitter V:

$$V_E^2(\vec{r},\omega) = \frac{4}{\pi}\omega\mathrm{Im}[\varepsilon(\vec{r},\omega)]\Theta\left(\omega,T(\vec{r})\right), \quad (6)$$

where $\Theta\left(\omega,T(\vec{r})\right)$ is the Planck term:

$$\Theta\left(\omega,T(\vec{r})\right) = \frac{\hbar\omega}{\exp\left(\frac{\hbar\omega}{\mathrm{k_B}T(\vec{r})}\right)-1}, \quad (7)$$

with $\hbar$ and $\mathrm{k_B}$ representing the reduced Planck constant and the Boltzmann constant, respectively. In Eqs. (5) and (6), the spatial inhomogeneities in both the permittivity and

temperature can be captured by the V_E^2 term. Therefore, by considering the spatial variance of V_E^2, one can treat the two kinds of spatial inhomogeneities equally.

Unlike the conventional WCE method [27], the spatially dependent V_E^2 term in inhomogeneous cases needs to be taken care of before the thermal current can be expanded. Since V_E^2 is nonzero, it can be divided to the left-hand side of Eq. (5) and be moved into the bra-ket because it is deterministic. By defining a new vector $\vec{\xi} = \vec{j}(\vec{r}, \omega)/V_E$, Eq. (5) can be re-written as:

$$\langle \vec{\xi}(\vec{r}_1, \omega)\vec{\xi}^*(\vec{r}_2, \omega)\rangle = \delta(\vec{r}_1 - \vec{r}_2)\boldsymbol{I}. \tag{8}$$

The delta function on the right-hand side of Eq. (8) implies $\vec{\xi}$ can be expressed by a linear superposition of the white noise function $\mathrm{d}W(\vec{r})$:

$$\vec{\xi}(\vec{r}) = \sum_{m\in\{x,y,z\}} \mathrm{d}W_m(\vec{r})\vec{e}_m\,, \tag{9}$$

where $\vec{e}_m$ is the directional vector in the m direction.

According to the Karhunen-Loève theorem [36], the white noise function $\mathrm{d}W$ can be expanded into a set of pre-determined complete and orthonormal basis functions defined within the emitter V:

$$\mathrm{d}W_m(\vec{r}) = \sum_{\alpha=1}^{\infty} c_{m\alpha} f_\alpha(\vec{r}), \tag{10}$$

where f_α are the set of basis functions labeled by the mode index α, which follow:

$$\int_V f_\alpha(\vec{r}) f_\beta^*(\vec{r})\mathrm{d}\vec{r} = \delta_{\alpha\beta}, \tag{11}$$

and $c_{m\alpha}$ are the expansion coefficients that obey:

$$\langle c_{m\alpha}\rangle = 0 \qquad \langle c_{m\alpha}c_{n\beta}\rangle = \delta_{mn}\delta_{\alpha\beta}. \tag{12}$$

Substituting Eq. (10) into Eq. (9), the current source $\vec{j}$ can be expressed as

$$\vec{j}(\vec{r},\omega) = \sum_{m\in\{x,y,z\}} \sum_{\alpha=1}^{\infty} c_{m\alpha}\, V_E(\vec{r},\omega) f_\alpha(\vec{r})\vec{e}_m, \tag{13}$$

and consequently,

$$\langle \vec{j}(\vec{r}_1,\omega)\vec{j}^*(\vec{r}_2,\omega)\rangle = \sum_{\alpha} V_E^2 f_\alpha(\vec{r}_1) f_\alpha^*(\vec{r}_2)\boldsymbol{I}\,. \tag{14}$$

Plugging Eq. (14) into Eq. (3), the Poynting vector can now be expressed in a summation form:

$$\begin{aligned}\langle P_k(\vec{r}_0,\omega)\rangle &= \varepsilon_{ijk}\cdot i\mu_0\omega \int_V \mathrm{d}\vec{r}_1 \int_V \mathrm{d}\vec{r}_2 \mathrm{Tr}\left[G_i^{E*} G_j^H \sum_\alpha V_E^2\, f_\alpha(\vec{r}_1) f_\alpha^*(\vec{r}_2)\boldsymbol{I}\right] \\ &= \sum_\alpha \sum_{m\in\{x,y,z\}} \varepsilon_{ijk}\cdot i\mu_0\omega \int_V \mathrm{d}\vec{r}_1 \int_V \mathrm{d}\vec{r}_2 \mathrm{Tr}\left[G_i^{E*} G_j^H \vec{J}_{\alpha,m}\vec{J}_{\alpha,m}^*\right] \\ &= \sum_\alpha \sum_{m\in\{x,y,z\}} \mathrm{L_P}\left[V; \vec{J}_{\alpha,m}\vec{J}_{\alpha,m}^*\right],\end{aligned} \tag{15}$$

where $\vec{J}_{\alpha,m}$ represents the current mode defined by f_α:

$$\vec{J}_{\alpha,m}(\vec{r},\omega) = V_E(\vec{r},\omega)\cdot f_\alpha(\vec{r})\vec{e}_m, \qquad m\in\{x,y,z\}. \tag{16}$$

According to the definition of the operator $\mathrm{L_p}[\Omega; X]$, each term of the summation in Eq. (15) represents the Poynting vector emitted by the emitter V when it is excited by the current mode $\vec{J}_{\alpha,m}$, defined in Eq. (16). Therefore, in order to evaluate the thermal emission of an emitter, one can excite the emitter by a series of current modes $\vec{J}_{\alpha,m}$, then calculate and sum all the corresponding Poynting vectors. The calculation usually converges quickly over the first several modes [37].

3. Implementation of the WCE method

To implement the WCE method, we choose Finite-difference Time-domain (FDTD) electromagnetic solvers because FDTD enables defining deterministic current modes in space. For cuboid emitters, the current modes can be defined by the Fourier series [27]. For the emitters with other geometries, the current modes can be generated through performing the Gram-Schmidt orthonormalization [38] to any set of complete basis functions. The current modes can also be approximated by a series of electrical dipoles via the discrete dipole approximation (DDA) [27,39]. After defining the current modes, the Poynting vectors are calculated to generate the thermal radiation spectrum.

Theoretically, the above-mentioned process can be done for any emitters if the V_E term in Eq. (16) is known. However, this may not be straightforward when the V_E term is a function of both the space and frequency, because it is not always possible to specify the features of the sources in both the space and frequency domains in FDTD solvers. For instance, we implement the WCE method in the Ansys Lumerical FDTD-solutions with DDA, where only the locations and magnitudes of the dipoles can be specified. To solve this problem, we make the approximation $V_E(\vec{r},\omega) \approx V_1(\vec{r})V_2(\omega)$ when V_E is not variable separable. This approximation can be justified through the frequency domain implementation of the WCE method, as we will discussed later. With this approximation, Eq. (16) can be expressed as:

$$\vec{j}_{\alpha,m}(\vec{r},\omega) = V_E(\vec{r},\omega)\cdot f_\alpha(\vec{r})\vec{\mathrm{e}}_\mathrm{m} \approx V_1(\vec{r})f_\alpha(\vec{r})\vec{\mathrm{e}}_\mathrm{m}\cdot V_2(\omega)$$
$$\equiv \tilde{j}_{\alpha,m}(\vec{r})V_2(\omega), \qquad (17)$$

where $\tilde{j}_{\alpha,m}(\vec{r})$ is the vectoral current density in the direction of $\vec{\mathrm{e}}_\mathrm{m}$ and characterizes the mode α

in the spatial domain only. According to Eq. (15), the Poynting vector arising from the mode $\vec{J}_{\alpha,m}$ can be expressed as:

$$\langle P_k(\vec{r}_0,\omega)\rangle_\alpha = \sum_{m\in\{x,y,z\}} \varepsilon_{ijk}\cdot i\mu_0\omega \int_V \mathrm{d}\overrightarrow{r_1}\int_V \mathrm{d}\overrightarrow{r_2}\mathrm{Tr}\left[G_i^{E*}G_j^H\tilde{J}_{\alpha,m}\tilde{J}_{\alpha,m}^*\right]V_2^2(\omega)$$

$$= V_2^2(\omega)\sum_{m\in\{x,y,z\}} \mathrm{L_p}\left[V;\tilde{J}_{\alpha,m}\tilde{J}_{\alpha,m}^*\right]. \quad (18)$$

In Eq. (18), the $L_p[\cdot;\cdot]$ represents the radiative spectrum from non-disperse sources $\tilde{J}_{\alpha,m}$. Such a spectrum can be directly acquired from simulation when continuous wave normalization is used; the $V_2^2(\omega)$ term is then timed to the summation of the simulated spectra, $\sum_{m\in\{x,y,z\}}\mathrm{L_p}\left[V;\tilde{J}_{\alpha,m}\tilde{J}_{\alpha,m}^*\right]$, to incorporate the frequency domain features of the current sources and produce the actual thermal radiation spectrum.

In order to justify the approximation of the $V_E(\vec{r},\omega)$ term, a frequency domain implementation of the WCE method is also introduced. In this approach, the simulation is performed at each frequency of interest separately and thus bypass the difficulty of specifying the current modes in both the space and frequency domains. At a given frequency ω_i, the current source $\vec{J}_{\alpha,m}(\vec{r},\omega_i)$ defined in Eq. (16) is a space-dependent function only and thus can be implemented without any approximation. However, the frequency domain implementation requires running the simulation multiple times and hence a longer simulation time. The results from the two methods match with each other with a minor discrepancy near the resonance frequency (see Section 4.2), which proves that our approximation is valid. Despite this minor numerical discrepancy, the variable separation approximation realizes the time-domain implementation of the inhomogeneous WCE method and thus significantly improves the simulation efficiency, since the spectrum in the time-domain simulation is calculated via the Fourier transformation

from a time-domain signal, instead of being simulated at each frequency separately. A frequency domain simulation can then be conducted near the resonance frequency to eliminate the possible numerical errors if a more precise value of the resonant magnitude is demanded.

4. Results and discussion

4.1. Validation of the inhomogeneous WCE method

Here we verify the inhomogeneous WCE method against the traditional approach. An emitter with a piece-wisely homogeneous permittivity is considered. The emission field from this emitter can be solved in two ways: the inhomogeneous WCE method can be applied to the emitter globally to calculate its radiative spectrum $P_1(\omega)$; or in the traditional approach, the homogenous WCE method is applied to each homogenous subpart of the emitter individually. Because the thermal sources at different parts of the emitter are spatially uncorrelated, the radiative spectrum from each part should follow the additive principle (illustrated in Fig.1; see Appendix for a proof) and thus their superposition should match with $P_1(\omega)$, which will serve as the indicator for the validation of the inhomogeneous WCE method.

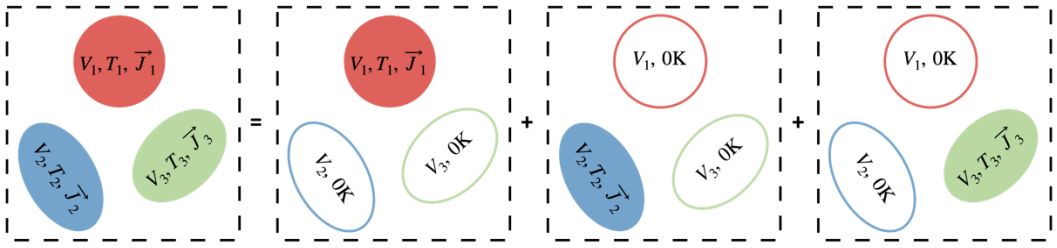

Figure 1. Schematic of the additive principle of thermal radiation. The thermal radiation from a system consisting of multiple emitters is equivalent to the superposition of the thermal radiation from each emitter excited individually to the same temperature as it is in the system. The excited emitters are marked by solid blocks.

Figure 2 (a) shows the schematic of the considered emitter in vacuum ($\varepsilon_r = 1$). To assign a piece-wisely homogeneous relative permittivity to the emitter, we define a global relative permittivity with a spatial dependent factor $\Xi(z)$:

$$\varepsilon_r(z,\omega) = \Xi(z)\cdot L(\omega), \qquad -\frac{t}{2} < z < \frac{t}{2}, \tag{19}$$

where t is the thickness of the emitter; $L(\omega) = 1 - \frac{\omega_p^2}{\omega^2 + i\gamma\omega}$, with $\omega_p = 7\left(\frac{2\pi c}{a}\right)$ and $\gamma = 0.03\left(\frac{2\pi c}{a}\right)$, c representing the speed of light in vacuum, and $a = 1\mu m$. $\Xi(z) = 2 - \delta(z - |z|)$ is the spatially dependent factor, resulting in the piece-wisely homogeneous permittivity in the $z > 0$ and the $z < 0$ regions, respectively (see Fig.2(a) inset).

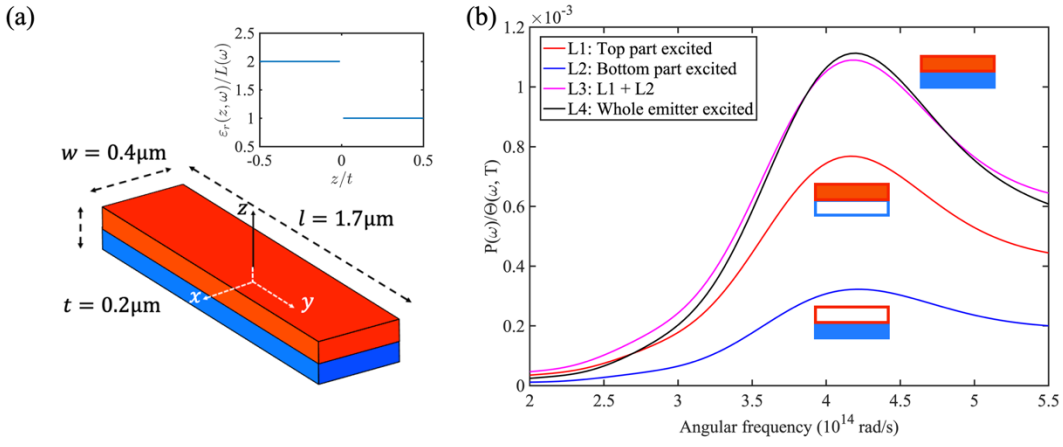

Figure 2. (a) Schematic of the slab emitter with inhomogeneous permittivity in the z direction. The center of the emitter is located at the origin. Inset: Piece-wisely homogeneous permittivity of the slab emitter. (b) Simulated radiative spectra of the slab emitter when the whole emitter is excited (black line) and only one homogeneous part is excited (red and blue lines). Excited parts are marked by solid rectangles.

The simulated radiative spectra are shown in Fig. 2 (b). A resonance peak at $\omega_0 = 4.3 \times 10^{14}\mathrm{rad/s}$ is observed. The blue and red lines show the contributions when only one homogeneous part is excited in the conventional WCE method. The summation of these two, shown in the purple line, matches the result (black line) obtained using the inhomogeneous WCE method applied to the entire inhomogeneous emitter, which validates our new formulations in inhomogeneous cases.

As shown in this example, the inhomogeneous WCE method provides the same results produced by the traditional approach and improves the time efficiency. Such the improvement is achieved through embedding the inhomogeneous information of the emitter into the current modes, as shown in Eq. (16), which enables us simulating the radiation from an inhomogeneous material using the spatially variant V_E^2 term. Hence, the inhomogeneous problem can be solved in one simulation, rather than being divided into several homogeneous problems. Applying the inhomogeneous WCE method will be more helpful when the permittivity or temperature of the simulated emitter is continuously varied in space, because in such cases, the conventional approach requires a fine discretization of the emitter in space so that each part can be approximated to be homogeneous, which will dramatically increase the total simulation time.

4.2. Temperature inhomogeneity in near field radiative heat transfer

Here, we demonstrate the applicability of the inhomogeneous WCE method under nonuniform temperature with a near field radiative heat transfer example. The radiative heat transfer between a pair of emitter and absorber with uniform temperatures T_E and T_A, respectively, are usually formulated as [40,41]

$$q = \int_0^\infty \mathrm{P}(\omega)\mathrm{d}\omega = \int_0^\infty \Phi(\omega)[\Theta(\omega, T_E) - \Theta(\omega, T_A)]\,\mathrm{d}\omega, \quad (20)$$

which is mainly influenced by the ensemble averaged flow spectrum $\Phi(\omega)$ of the emitter-absorber system (regulated by the geometry and material property) and the temperature difference between the emitter and the absorber (captured by the difference of the Planck terms). However, the influence of the temperature gradient in emitters or absorbers has rarely been studied. To demonstrate this, we studied the near field radiative heat transfer between two gold nanorods (GNRs) when nonuniform temperature profiles are considered. The layout of the GNRs is shown in Fig. 3 (a), where the two GNRs are parallel to each other with a gap distance $d = 50$ nm and the length l of 1.5μm, and the cross-sectional shape is a square with the side length s of 50 nm. The temperature of the GNR absorber is kept at $T_A = 0$K for simplicity, whereas the GNR emitter is assumed to have a linear temperature profile in the x direction

$$T(x) = T_c - (T_c - T_e)\frac{2|x - x_0|}{l}, \quad (21)$$

where x_0 represents the central location of the emitter, T_c and T_e represent the temperatures at the center and each end of the emitter, respectively. Two specific non-uniform cases are considered: 1. $T_c = 1000$K and $T_e = 400$K (center high, CH); 2. $T_c = 400$ K and $T_e = 1000$K (center low, CL). In both the cases, the linear temperature distribution results in an average temperature

difference between the emitter and the absorber $\Delta T = \int_V (T(x) - T_A)\mathrm{d}x\,/V = 700$ K. Hence, a GNR emitter with the uniform temperature $T_0 = \Delta T$(i.e., $T_c = T_e = T_0$) is also studied as a reference. In all three cases, the permittivity of gold is assumed to be temperature independent.

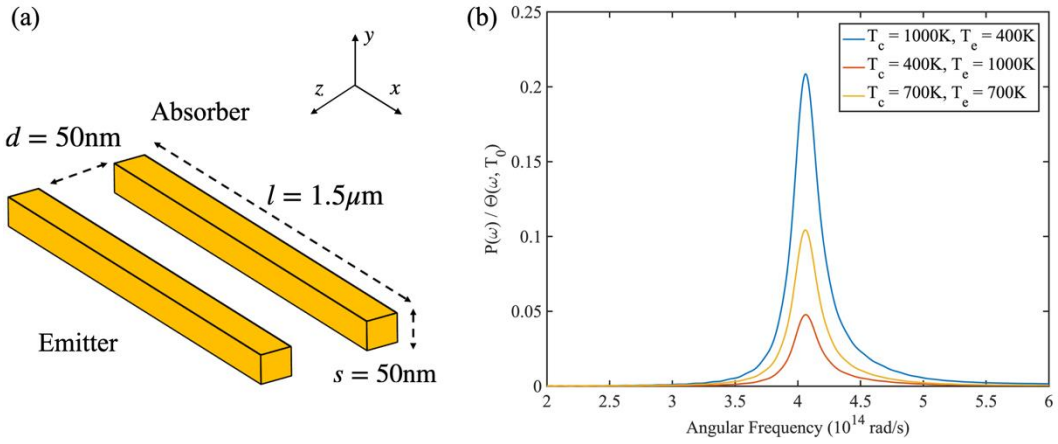

Figure 3. (a) Schematic of the layout of the simulated gold nanorods (GNRs). The absorber is kept at 0K, whereas a linear temperature profile is assumed for the emitter. (b) Simulated radiative spectra between the GNR emitters with different temperature profiles and the 0K GNR absorber. A four-time tunability in the resonance magnitude is achieved by imposing the center-high (blue line) and the center-low (red line) temperature profiles.

The simulated radiative heat transfer spectra for the three above-mentioned cases are plotted in Fig. 3 (b). Resonant peaks centered at $\omega = 4.05 \times 10^{14}\mathrm{rad/s}$ are observed in all the cases, corresponding to the longitudinal localized surface plasmon resonance (LSPR) of GNRs [33]. The magnitudes of the LSPR in these cases, however, differ from each other. Compared to the reference case where the temperature of the emitter is uniform (yellow line), the resonance peak height in the radiative heat transfer spectra is doubled for the CH case (blue line) and reduced by

half for the CL case (red line), resulting in a four-time tunability in the spectra of the near field radiative spectra.

Note that the simulated spectra shown in Fig. 3(b) are generated with the approximation of $V_E(\vec{r},\omega) \approx V_1(\vec{r})V_2(\omega)$ as discussed in Section 3, where V_1 and V_2 are acquired through a gradient descent process to minimize the loss function $\mathcal{L} = \int d\vec{r} \int \mathrm{d}\omega |V_E - V_1 V_2|^2$. Specifically, for the GNR emitter with the CH temperature profile, we choose:

$$V_1 = \sqrt{\frac{3}{5}\left(\frac{T(x)}{\mathrm{T_{eff}}}\right)^3 + \frac{2}{5}\left(\frac{T(x)}{\mathrm{T_{eff}}}\right)^2}, \tag{22}$$

and

$$V_2 = \sqrt{\Theta(\omega, \mathrm{T_{eff}})}, \tag{23}$$

with $\mathrm{T_{eff}} = 900\mathrm{K}$.

To validate the approximation mentioned above, we also implemented the inhomogeneous WCE method in the frequency domain for the case with CH temperature profile without any approximation of V_E. Figure 4 shows the simulated spectra from the two approaches of the near field radiative heat transfer between the above-mentioned CH emitter and the 0K GNR absorber. The two results match well with each other except for a minor difference in the resonant magnitude caused by the approximation of the V_E term.

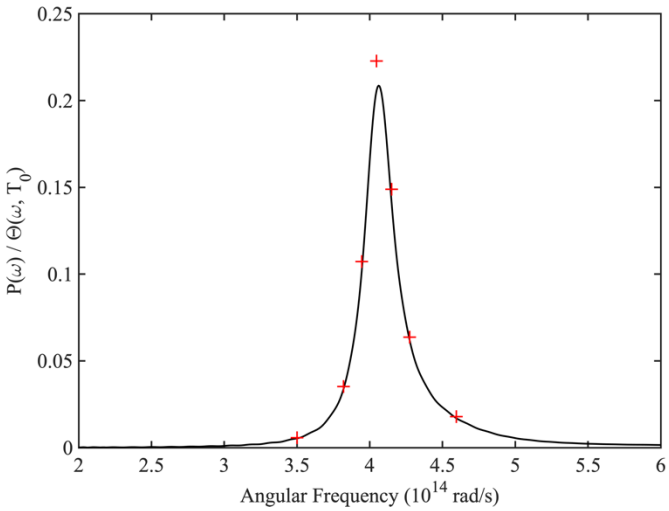

Figure 4. Comparison of the simulation results performed by the inhomogeneous WCE method implemented with the variable separation approximation of V_E(black line) and at each frequency separately (red crosses). The result shows the CH case.

To further illustrate the role that the temperature profile plays in the near field radiative heat transfer, $|E|^2$ profiles at the resonance frequency for the above-mentioned cases are plotted in Figs. 5 (a), (b) and (c) by the same color scale. Despite the difference in magnitude, the near field radiation in the three cases follows the same dipole-like mode, which is also manifested by the identical relative field profiles along the three white dash lines (field profile along each line normalized to its own maximum), as shown in Fig. 5 (d). Therefore, instead of altering the resonant mode of the GNR systems, the temperature profile serves as an independent factor to modulate the magnitude of the resonance of the GNRs, and results in the increased peak height in the CH case (Fig. 5 (a)) and decreased peak height in the CL case (Fig. 5 (b)), compared to the uniform case (Fig. 5 (c)). However, understanding the detailed mechanism of the magnitude

modulation and determining the optimized temperature profiles to maximize or minimize the near field radiative heat transfer need further investigations.

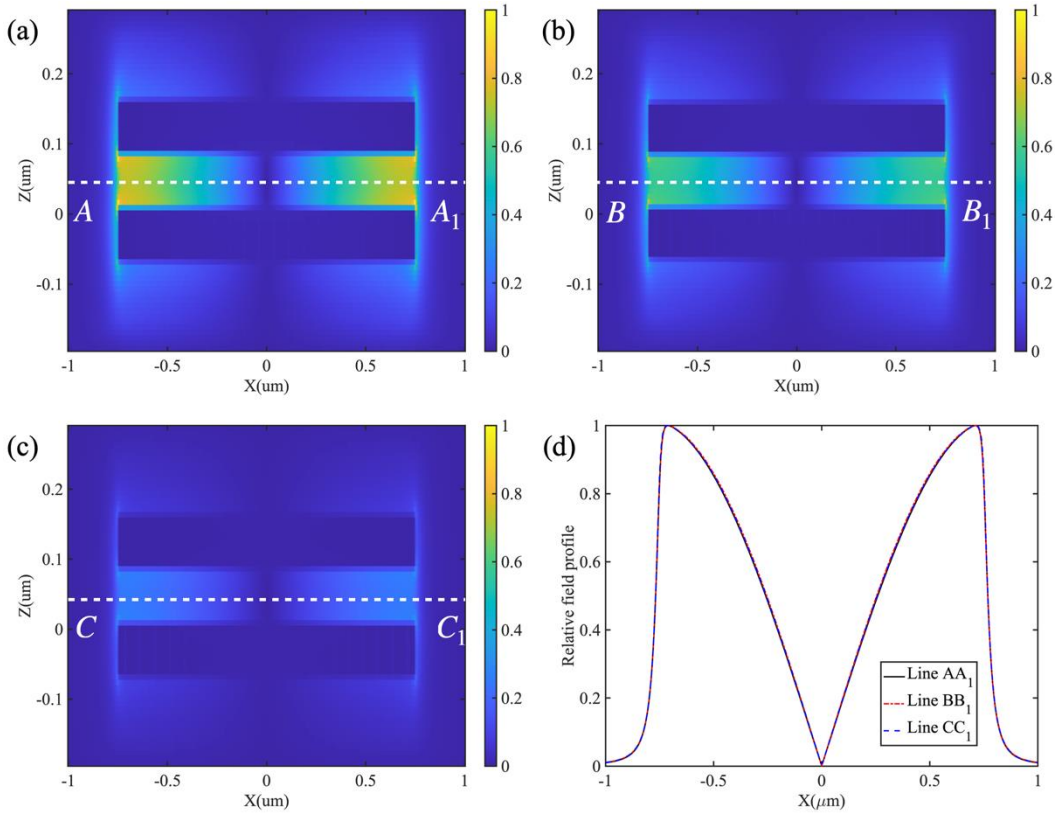

Figure 5. $|E|^2$ profiles (arb. units) at the resonance frequency plotted in the same color scale when the GNR emitter is assumed to have the (a) center-high, (b) uniform and (c) center-low temperature profiles. (d) Relative field profiles along the three white dashed lines in (a), (b) and (c). The identical relative field profiles prove that the three cases share the same dipole mode, and different temperature profiles affect the magnitude of the resonance independently.

5. Conclusion

We generalize the formulism of the WCE method for a time-efficient calculation of thermal radiation in inhomogeneous systems and validate our method via a slab emitter with piece-wisely

homogeneous permittivity. The new formalism treats the inhomogeneity in the primitivity or temperature with the same set of formula and thus provides a systematic method to study the systems with the two kinds of inhomogeneity. The inhomogeneous information of the structures is embedded into the current modes via the spatially variant V_E^2 term, which improves the time efficiency when compared to traditional approaches where the inhomogeneous structures are approximated by the superposition of their quasi-homogenous subparts. Our new method may also be applied to spatially disordered system [42–44] if the spatial coherence/correlation feature is considered while generating current modes, which we will investigate in future studies. We apply our method to study the near field radiative heat transfer between two GNRs and achieve a four-time tunability in the magnitude of the LSPR when different temperature profiles are assigned to the emitter. The results clearly show the significance of the detailed temperature profile, which, in addition to the temperature difference and the resonance mode, serves as another independent factor to modulate the near field radiative heat transfer and thus may provide an extra degree of freedom to tailor thermal radiation.

Appendix

Additive principle for the thermal radiation. Consider a system consisting of a series of emitters labeled by the index i; the volumes of the emitters are noted as V_i, and define $V = \cup V_i$. All the emitters are at their own thermal equilibrium, that is, they have well-defined temperature T_i and permittivity ε_i. To find the Poynting vector emitted by the system, define operator $R_i(\vec{r})$:

$$R_i(\vec{r}) = \begin{cases} 1, & \vec{r} \in V_i \\ 0, & \vec{\mathrm{r}} \notin V_i \end{cases}, \tag{24}$$

then the thermal current distribution among the system can be expressed as:

$$\vec{J}(\vec{r}) = \sum_i \vec{J}_i(\vec{r}) R_i(\vec{r}), \tag{25}$$

where $\vec{J_i}$ is the current distribution inside object i, which follows the FDT as shown in Eqs. (4) and (5).

The Poynting vector emitted by the system can be expressed as:

$$\begin{aligned} P(\vec{r}_0, \omega) &= \mathrm{L_p}\left[\cup V_i;\ \langle \sum_i \vec{J}_i(\vec{r}_1, \omega) R_i(\vec{r}_1) \sum_k \vec{J}_k^*(\vec{r}_2, \omega) R_k(\vec{r}_2)\rangle\right] \\ &= \sum_i \mathrm{L_P}[V_i; \langle \vec{J}_i(\vec{r}_1, \omega) \vec{J}_i^*(\vec{r}_2, \omega)\rangle] \\ &+ \sum_{i \neq k} \mathrm{L_p}[V_i \cup V_k; \langle \vec{J}_i(\vec{r}_1, \omega) \vec{J}_k^*(\vec{r}_2, \omega) R_i(\vec{r}_1) R_k(\vec{r}_2)\rangle], \end{aligned} \tag{26}$$

For the second term on the right-hand side (RHS), the $R_i \cdot R_k$ term varnishes except for the case when $\overrightarrow{r_1} \in V_i$ and $\overrightarrow{r_2} \in V_k$, which results in $\langle \vec{J}_i \cdot \vec{J}_k^* \rangle = 0$, according to FDT. Therefore, the second term on the RHS of Eq. (26) varnishes, and the Poynting vector emitted by the system can be simplified as:

$$\begin{aligned} P(\vec{r}_0, \omega) &= \sum_i \mathrm{L_P}[V_i; \langle \vec{J}_i(\vec{r}_1, \omega) \vec{J}_i^*(\vec{r}_2, \omega)\rangle] \\ &\equiv \sum_i P_i\ , \end{aligned} \tag{27}$$

where P_i represents the Poynting vector emitted by the system when only emitter i is excited.

Data availability: The data that support the findings of this study are available from the corresponding authors upon reasonable request.

Corresponding Author

*E-mail: sshen1@cmu.edu

Author Contributions

The manuscript was primarily written by the first author Z. Li while other authors provided suggestions and revisions. All authors have given approval to the final version of the manuscript. S. Shen supervised the research.

Notes

The authors declare no competing financial interest.

Acknowledgments

This work was primarily supported by the Defense Threat Reduction Agency (Grant no. HDTRA1-18-1-0046). This work was also funded partially by the National Science Foundation (Grant no. CBET-1931964) and the CMU-Portugal Program.

References

1. S. A. Maier, *Plasmonics: Fundamentals and Applications* (Springer, New York, NY, 2007).

2. P. Biagioni, J.-S. Huang, and B. Hecht, Reports on Progress in Physics **75**, 024402 (2012).

3. S. Shin, M. Elzouka, R. Prasher, and R. Chen, Nature Communications **10**, 1377 (2019).

4. J. Li, J. Wuenschell, Y. Jee, P. R. Ohodnicki, and S. Shen, Physical Review B **99**, 235414 (2019).

5. B. Sepúlveda, P. C. Angelomé, L. M. Lechuga, and L. M. Liz-Marzán, Nano Today **4**, 244 (2009).

6. T. Inoue, M. de Zoysa, T. Asano, and S. Noda, Optica **2**, 27 (2015).

7. B. Zhao, P. Santhanam, K. Chen, S. Buddhiraju, and S. Fan, Nano Letters **18**, 5224 (2018).

8. A. Lenert, D. M. Bierman, Y. Nam, W. R. Chan, I. Celanović, M. Soljačić, and E. N. Wang, Nature Nanotechnology **9**, 126 (2014).

9. M. Laroche, R. Carminati, and J. J. Greffet, Journal of Applied Physics **100**, 063704 (2006).

10. S. Molesky and Z. Jacob, Physical Review B - Condensed Matter and Materials Physics **91**, 205435 (2015).

11. B. Zhao, P. Santhanam, K. Chen, S. Buddhiraju, and S. Fan, Nano Letters **18**, 5224 (2018).

12. Q. Ni, R. Ramesh, C.-A. Chen, and L. Wang, Optics Letters **46**, 3163 (2021).

13. Q. Ni, R. McBurney, H. Alshehri, and L. Wang, Solar Energy **191**, 623 (2019).

14. Y. de Wilde, F. Formanek, R. Carminati, B. Gralak, P. A. Lemoine, K. Joulain, J. P. Mulet, Y. Chen, and J. J. Greffet, Nature **444**, 740 (2006).

15. A. Babuty, K. Joulain, P. O. Chapuis, J. J. Greffet, and Y. de Wilde, Physical Review Letters **110**, 146103 (2013).

16. A. v. Shchegrov, K. Joulain, R. Carminati, and J. J. Greffet, Physical Review Letters **85**, 1548 (2000).

17. L. Eyges, *The Classical Electromagnetic Field* (Dover Publications, New York, NY, 1972).

18. S. I. Maslovski, C. R. Simovski, and S. A. Tretyakov, Physical Review B - Condensed Matter and Materials Physics **87**, 155124 (2013).

19. L. Zhu, S. Sandhu, C. Otey, S. Fan, M. B. Sinclair, and T. S. Luk, Applied Physics Letters **102**, (2013).

20. B. Liu, W. Gong, B. Yu, P. Li, and S. Shen, Nano Letters **17**, 666 (2017).

21. E. S. C. Ching, P. T. Leung, A. Maassen Van Den Brink, W. M. Suen, S. S. Tong, and K. Young, Reviews of Modern Physics **70**, 1545 (1998).

22. J. Li, Z. Li, and S. Shen, Optics Express **28**, 34123 (2020).

23. G. T. Horowitz and V. E. Hubeny, Physical Review D - Particles, Fields, Gravitation and Cosmology **62**, 024027 (2000).

24. A. W. Rodriguez, M. T. H. Reid, and S. G. Johnson, Physical Review B - Condensed Matter and Materials Physics **88**, 054305 (2013).

25. A. W. Rodriguez, M. T. H. Reid, and S. G. Johnson, Physical Review B - Condensed Matter and Materials Physics **86**, 220302(R) (2012).

26. B. Liu and S. Shen, Physical Review B - Condensed Matter and Materials Physics **87**, 115403 (2013).

27. J. Li, B. Liu, and S. Shen, Physical Review B **96**, 075413 (2017).

28. S. B. Wen, Journal of Heat Transfer **132**, 072704 (2010).

29. R. St-Gelais, L. Zhu, S. Fan, and M. Lipson, Nature Nanotechnology **11**, 515 (2016).

30. J. Li, B. Yu, and S. Shen, Physical Review Letters **124**, 137401 (2020).

31. J. Song, Q. Cheng, Z. Luo, X. Zhou, and Z. Zhang, International Journal of Heat and Mass Transfer **140**, 80 (2019).

32. C. R. Otey, L. Zhu, S. Sandhu, and S. Fan, Journal of Quantitative Spectroscopy and Radiative Transfer **132**, 3 (2014).

33. J. Li, J. Wuenschell, Z. Li, S. Bera, K. Liu, R. Tang, H. Du, P. R. Ohodnicki, and S. Shen, Small **2007274**, 2007274 (2021).

34. A. G. Polimeridis, M. T. H. Reid, W. Jin, S. G. Johnson, J. K. White, and A. W. Rodriguez, Physical Review B - Condensed Matter and Materials Physics **92**, 134202 (2015).

35. L. D. Landau and E. M. Lifshitz, *Statistical Physics. Course of Theoretical Physics*, 3rd ed. (1980).

36. R. Ghanem and P. Spanos, *Stochastic Finite Elements: A Spectral Approach* (Springer-Verlag, 1991).

37. S. P. Huang, S. T. Quek, and K. K. Phoon, International Journal for Numerical Methods in Engineering **52**, 1029 (2001).

38. W. Cheney and D. Kincaid, *Linear Algebra: Theory and Applications* (Jones and Bartlett, Sudbury, Ma, 2009).

39. E. Tervo, M. Francoeur, B. Cola, and Z. Zhang, Physical Review B **100**, 205422 (2019).

40. Z. M. Zhang, *Nano and Microscale Heat Transfer* (2020).

41. S. Basu, Z. M. Zhang, and C. J. Fu, Int. J. Energy Res **33**, 1203 (2009).

42. A. Cazé, R. Pierrat, and R. Carminati, Physical Review Letters **110**, 063903 (2013).

43. V. Krachmalnicoff, E. Castanié, Y. de Wilde, and R. Carminati, Physical Review Letters **105**, 183901 (2010).

44. W. J. M. Kort-Kamp, P. I. Caneda, F. S. S. Rosa, and F. A. Pinheiro, Physical Review B - Condensed Matter and Materials Physics **90**, 140202(R) (2014).